Editors' Suggestion

Experimental Realization of a Three-Dimensional Dirac Semimetal Phase with a Tunable Lifshitz Transition in Au_2Pb

J. Sánchez-Barriga[1,2,*] O. J. Clark[1] M. G. Vergniory[3,4] M. Krivenkov[1]
A. Varykhalov[1] O. Rader[1] and L. M. Schoop[5]

[1]*Helmholtz-Zentrum Berlin für Materialien und Energie, Albert-Einstein-Strasse 15, 12489 Berlin, Germany*
[2]*IMDEA Nanoscience, C/ Faraday 9, Campus de Cantoblanco, 28049 Madrid, Spain*
[3]*Donostia International Physics Center, 20018 Donostia-San Sebastián, Spain*
[4]*Max Planck Institute for Chemical Physics of Solids, Dresden D-01187, Germany*
[5]*Department of Chemistry, Princeton University, Princeton, 08544 New Jersey, USA*

Three-dimensional Dirac semimetals are an exotic state of matter that continue to attract increasing attention due to the unique properties of their low-energy excitations. Here, by performing angle-resolved photoemission spectroscopy, we investigate the electronic structure of Au_2Pb across a wide temperature range. Our experimental studies on the (111)-cleaved surface unambiguously demonstrate that Au_2Pb is a three-dimensional Dirac semimetal characterized by the presence of a bulk Dirac cone projected off-center of the bulk Brillouin zone (BZ), in agreement with our theoretical calculations. Unusually, we observe that the bulk Dirac cone is significantly shifted by more than 0.4 eV to higher binding energies with reducing temperature, eventually going through a Lifshitz transition. The pronounced downward shift is qualitatively reproduced by our calculations indicating that an enhanced orbital overlap upon compression of the lattice, which preserves C_4 rotational symmetry, is the main driving mechanism for the Lifshitz transition. These findings not only broaden the range of currently known materials exhibiting three-dimensional Dirac phases, but also show a viable mechanism by which it could be possible to switch on and off the contribution of the degeneracy point to electron transport without external doping.

Three-dimensional Dirac semimetals host fourfold degenerate gapless crossing points, or "bulk Dirac cones" (BDCs), within their electronic structures [1]. These Dirac cones are three-dimensional analogs to those found in graphene. Accordingly, the material properties bestowed by BDCs when they cross the Fermi energy are unusual, from extremely high carrier mobility and larger transversal magnetoresistance to negative longitudinal magnetoresistance [2–8], all of which are highly desirable for next-generation spin and electronic applications [9].

In the case of twofold degenerate two-dimensional Dirac cones such as those found in graphene, any perturbation proportional to the third Pauli matrix, σ_z, such as spin-orbit coupling (SOC) or sublattice symmetry breaking, will always contribute a band gap to the Dirac cone [10–12]. In contrast, in stable three-dimensional Dirac cones, the addition or alteration of, e.g., SOC can always be compensated for by a crystal momentum, and therefore the crossing point simply moves along the momentum axis instead of becoming gapped [13]. Prominent examples of three-dimensional Dirac semimetals include Cd_2As_3 and Na_3Bi, which host symmetry-protected bulk Dirac points along their C_4 and C_3 symmetric k_z axes, respectively [3–8,14,15].

A continuously increasing number of materials hosting these lattice-symmetry protected crossing points are predicted theoretically, several of which have been experimentally confirmed [16–27]. However, in order to truly exploit the unique electronic properties of this type of material in real applications, one must find an instance of a system hosting bulk Dirac points in conjunction with an in-built mechanism by which their energetics can be tuned, or by which the crossing points can be switched on and off entirely by lifting the protective C_n symmetry. Among the different potential realizations of three-dimensional Dirac semimetals, Au_2Pb [28] is thought to be one candidate material suited to this purpose.

The cubic Laves compound Au_2Pb has been theoretically predicted to host a BDC with a fourfold degenerate crossing point that gaps upon cooling through several structural phase transitions below 100 K [28]. A subset of these low temperature phases are expected to break the C_4 rotational lattice symmetry that protects the three-dimensional Dirac crossing against opening a gap [28,29]. Intriguingly, the resulting band gap is predicted to be inverted with a topologically nontrivial $\mathbb{Z}_2$ index of -1 that persists as the system enters a superconducting phase below 1.2 K. Therefore, it has been suggested that Au_2Pb could be a potential material in which to realize the much sought after topological superconductivity [30], although as demonstrated in other systems, the mere coexistence

of the two phenomena is not necessarily a sufficient criterion [31,32].

Experimentally, however, very little is known about the electronic properties of Au_2Pb even in the intermediate temperature regime. From a photoemission perspective, previous angle-resolved photoemission (ARPES) experiments [33] performed at a fixed temperature (110 K) and photon energy using a helium discharge lamp, could not unambiguously confirm the existence of a BDC with a linear dispersion along all momentum directions in the high temperature phase. The lower temperature phases were left entirely unexplored. Here, we present a photon-energy and temperature dependent ARPES study on the (111)-cleaved surface of Au_2Pb. We explicitly verify the three-dimensional dispersion of the BDC in the high temperature cubic phase, and explore its evolution upon cooling into the intermediate temperature regime. Below 100 K, we find that the three-dimensional Dirac point does not open a gap indicating the continued presence of the protective C_4 rotational lattice symmetry. Rather, we find that the intact BDC significantly shifts to higher binding energies with reducing temperature, eventually undergoing a Lifshitz transition consistent with a compression of the lattice. Our present findings therefore provide direct evidence for both the unambiguous classification of Au_2Pb as a three-dimensional Dirac semimetal across a wide temperature range, and the presence of an intrinsic mechanism by which it is possible to tune highly conductive band features to the Fermi energy without external doping.

We performed photoemission experiments at temperatures between 38 and 300 K using linearly polarized undulator radiation at the U125-PGM beam line of BESSY-II. Photoelectrons were detected with a Scienta R4000 analyzer and the base pressure of the experimental setup was better than 1×10^{-10} mbar. Au_2Pb single crystals were grown out of Pb flux [28], and cleaved *in situ*. The high quality of the pristine Au_2Pb (111) surface was confirmed by scanning tunneling microscopy (STM) and low-energy electron diffraction (LEED), as seen in Figs. 1(a)–1(d). STM measurements were performed with an Omicron VT STM using polycrystalline tungsten tips prepared as described elsewhere [34]. Density functional theory (DFT) calculations including SOC were carried out within the full-potential linearized augmented-plane-wave formalism as implemented in the WIEN2k code [35].

Figures 1(a)–1(c) outline the structural quality of the pristine Au_2Pb (111) surface seen by STM. A perfectly periodic hexagonal lattice can be clearly observed in the STM images of Figs. 1(a) and 1(b). The hexagonal symmetry characteristic of the (111) surface can also be recognized in the distribution of well-defined diffraction spots seen in the LEED patterns of Fig. 1(d). From the STM images, as shown in the line profile of Fig. 1(c), we estimate a lateral periodicity $l \approx (5.70 \pm 0.05)$ Å which is in good agreement with the value of 5.63 Å found for the high
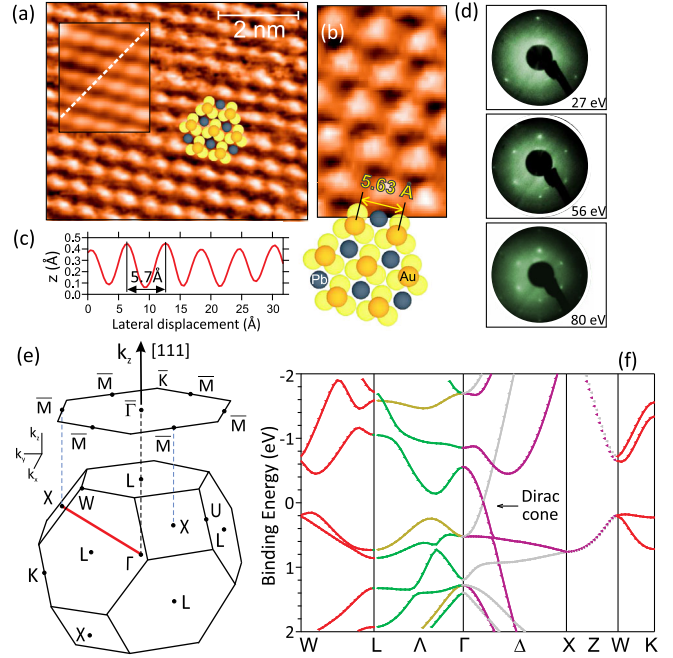
FIG. 1. (a)–(c) STM characterization of the pristine Au_2Pb (111) surface. (a) Atomically resolved I-channel STM image of the surface at room temperature (acquisition parameters: 0.3 V, 2 nA). Inset: Z-channel topography image (0.3 V, 0.5 nA). (b) Close view of the topography, I channel (0.3 V, 0.5 nA). A structural model is displayed as an overlay [yellow (gray) spheres represent Au (Pb) atoms]. (c) Line profile extracted along the white dashed line in (a). (d) Corresponding LEED patterns of the pristine Au_2Pb (111) surface acquired at different energies. (e) Sketch of the bulk and surface BZs of Au_2Pb (111). The red solid line indicates one of the six equivalent directions along which bulk Dirac points are predicted. (f) DFT band structure calculation over all high-symmetry directions of cubic Au_2Pb. The BDC is labeled, and band colors indicate different irreducible representations.

temperature phase at 298 K [36]. This correspondence is highlighted by a structural model, superimposed on the STM images of Figs. 1(a) and 1(b), that is also consistent with the measured average corrugation amplitude of (0.37 ± 0.06) Å in Fig. 1(c). The observed lateral periodicity yields an estimate of the lattice parameter $a = l\sqrt{2} \approx (8.06 \pm 0.07)$ Å which is in close agreement with the value of $a = 7.9603$ Å determined by x-ray diffraction in the cubic phase [36].

The corresponding hexagonal surface BZ is depicted in Fig. 1(e) alongside that of the bulk, showing one of the six equivalent Γ-X directions projecting onto $\bar{\Gamma}$-$\bar{M}$ along which fourfold degenerate, three-dimensional Dirac crossings are predicted [28]. There is considerable Pb p-derived orbital mixing over the entire energy range covered by our DFT calculations [Fig. 1(f)], but the necessary ingredients for the crossing itself stem from within the Au p-orbital manifold. A holelike $p_{x,y}$-derived band disperses linearly from low energy to high to cross through the oppositely dispersing p_z-derived band. The corresponding point group symmetry,

C_{4v}, in conjunction with SOC, results in a crossing between two bands of different irreducible representations, indicated by the band colors in Fig. 1(f), and thus, in the formation of a bulk Dirac point which is protected by C_4 crystalline symmetry. This can be seen in the DFT band structure calculation of Fig. 1(f), where the BDC, formed approximately one quarter of the way between Γ and X, is labeled. While the Dirac cones along Γ-X are the only bulk crossings connecting the valence and conduction bands across the otherwise continuous global band gap ($\mathbb{Z}_2 = -1$), we note that there are other electron and hole pockets which are energy degenerate with the Dirac points along the lower-symmetry Γ-K direction [28].

Unlike cases where the surface termination is along one of the cubic axes, where a pair of bulk Dirac crossings will always project onto the same position on the surface in momentum space, all the Dirac crossings on the (111) surface are well separated in momenta, and threefold rotationally symmetric along two distinct low-symmetry planes through the bulk BZ. In Fig. 2, we selectively probe one of these six equivalent BDCs, and measure its energy-momentum dispersion at 300 K along each of the orthogonal k_x, k_y, and k_z momentum directions indicated in Fig. 1(e). By performing ARPES measurements in a range of photon energies between 60 and 110 eV, we first explore the dispersion of the Dirac cone as a function of k_z [37]. Figures 2(a)–2(e) show representative band dispersions acquired along the projection onto the $\overline{\Gamma}$-$\bar{M}$ direction ($k_x = 0$ plane) at select k_z. The corresponding momentum-distribution curves are shown in Figs. 2(f)–2(j). The k_z dispersion of the BDC is clearly visible, proving its three-dimensional nature. The band dispersions in Figs. 2(c) and 2(h), where the largest momentum separation between the Dirac bands is seen, correspond to the location of the bulk Dirac point at $k_z = 0.13$ ΓL for 90 eV photons. For simplicity, the electron wave vectors are given relative to the absolute momentum positions of the bulk Dirac point, which resides at $k_x = 0$ and $k_y = 0.2$ $\overline{\Gamma M}$ in this low-symmetry plane. Figures 2(k)–2(m) show analogous k_x dispersions of the Dirac cone acquired at $k_z = 0.13$ ΓL along different k_y planes perpendicular to the projection onto the $\overline{\Gamma}$-$\bar{M}$ direction. A constant-energy contour of the BDC projected into k_z-k_y space ($k_x = 0$) at a binding energy of 0.38 eV is shown in Fig. 2(n). The linear band dispersions extracted from the experimental peak positions along all three momentum directions are summarized in Fig. 2(o), where an extrapolation of the Dirac dispersions gives a binding energy of the bulk Dirac point of $\approx(80 \pm 31)$ meV above the Fermi level. A slight anisotropy is visible along the k_z direction due to a reduced group velocity $v_z \approx (2.43 \pm 0.15)$ eV$\mathring{A}$ compared with the group velocities $v_x \approx (3.53 \pm 0.06)$ and $v_y \approx (3.57 \pm 0.06)$ eV$\mathring{A}$ along the k_x and k_y directions, respectively. The anisotropy is substantially smaller than that reported in the other three-dimensional
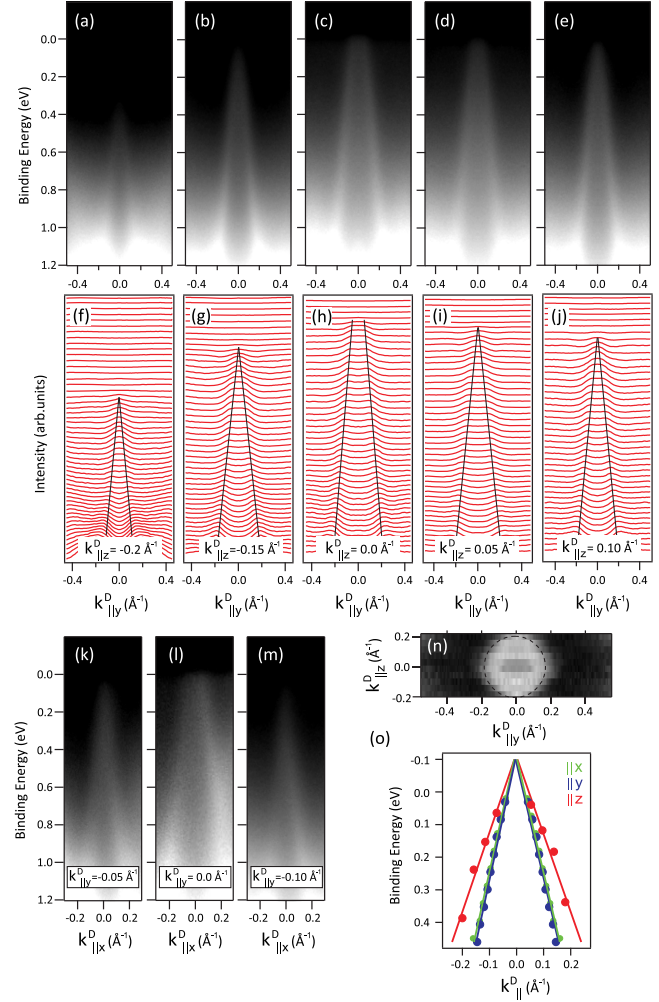
FIG. 2. (a)–(e) Band dispersions of the Dirac cone and (f)–(j) corresponding momentum-distribution curves (MDCs) acquired at 300 K along the k_y direction ($k_x = 0$ plane) at selected k_z. Black solid lines in (f)–(j) are guides to the eye, and electron wave vectors are given relative to the position of the bulk Dirac point. The MDCs shown span an energy range equivalent to that shown in (a)–(e). (k)–(m) Band dispersions acquired along different k_y planes parallel to the k_x direction, and at the k_z value corresponding to panels (c) and (h). (n) Constant-energy contour of the Dirac cone projected into k_z-k_y space ($k_x = 0$). (o) Linear dispersions of the Dirac bands along all three momentum directions.

Dirac semimetals such as Na$_3$Bi [4] and Cd$_3$As$_2$ [6], consistent with a cubic structure with a nearly spherical dispersion of the BDC in the vicinity of the Γ point.

Having demonstrated linear dispersion along different momentum directions and the three-dimensional nature of the Dirac cone, we next explore the evolution of the Dirac cone as a function of lattice temperature. In Figs. 3(a) and 3(b), we perform temperature dependent ARPES measurements along the projection onto the $\overline{\Gamma}$-$\bar{M}$ direction with the orthogonal electron wave vectors centered at the position of the bulk Dirac point in three-dimensional
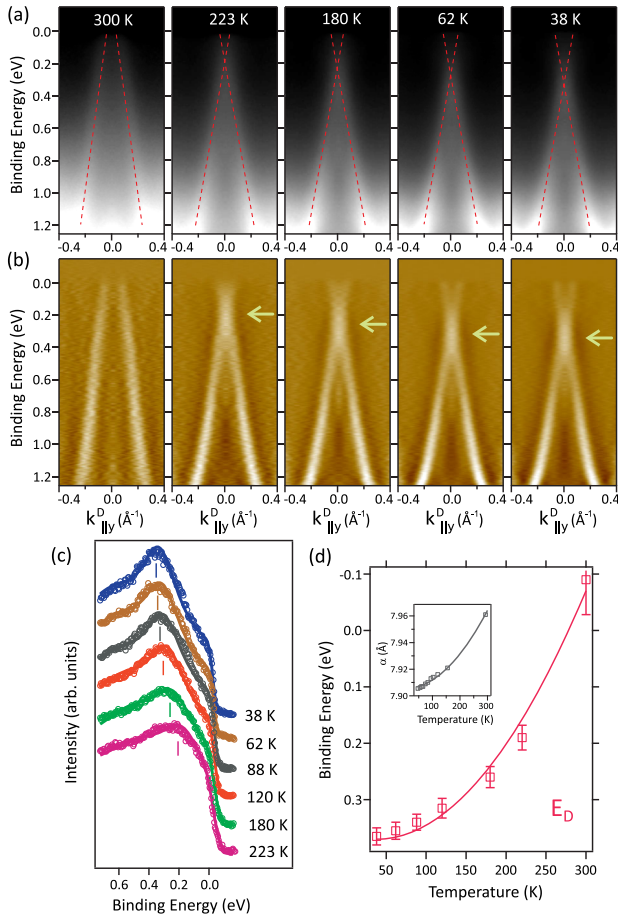
FIG. 3. (a) Band dispersions and (b) corresponding second derivative of the photoemission intensities of the Dirac cone at indicated temperatures. Red dashed lines in (a) are fits to the band dispersions tracing the temperature evolution of the Dirac cone and intersect at the bulk Dirac point, which shifts in energy with decreasing lattice temperature as emphasized by the horizontal arrows in (b). (c) Energy-distribution curves (open circles) and corresponding fits (solid lines) across the position of the bulk Dirac point at several temperatures. (d) Dependence of the Dirac point energy and lattice parameter (inset, derived from the data shown in [28]) with temperature. Solid lines are fits to the experimental data.

FIG. 4. (a)–(d) DFT band structure calculations showing a significant energy shift of the BDC upon compression of the lattice. Horizontal green lines mark the energy positions of the bulk Dirac point, and the lattice compressions $\Delta\epsilon$ are (a) 0%, (b) 0.8%, (c) 1.2%, and (d) 2.6%. Band colors indicate different irreducible representations. (e) Calculated dependence of the Dirac point energy with lattice compression.

momentum space. We observe that the BDC is significantly shifted to higher binding energies with reducing temperature, eventually going through a Lifshitz transition [38]. Unusually, the large energy shift can also be seen in the energy-distribution curves of Fig. 3(c) despite the steep linear dispersion near the Dirac crossing and the relative intensity contributions from Au d-like bulk states at higher binding energies.

In order to determine the origin of the observed Lifshitz transition, we consider the structural evolution of the lattice with reducing temperature. The band crossings of interest in Au$_2$Pb, driven by the crossing of orthogonal Au p_z- and $p_{x,y}$-derived wave functions along the C_4 rotational symmetric axes, are analogous to those formed across the C_3

symmetric transition metal dichalcogenides [39–43] and in other metallic and semimetallic C_3 and C_4 symmetric systems [26,44]. In those systems, due to the localization of the band crossings to within a single-orbital manifold, the application of large C_n preserving perturbations to the lattice is not sufficient to unwind the band crossings, instead simply acting to move the bulk Dirac points in energy and momentum. Only by lifting the protective C_n symmetry can a Dirac point be removed [26,40,45,46].

The perseverance of the bulk Dirac point in Au$_2$Pb over such a large temperature range, as shown in Figs. 3(a) and 3(b), is therefore indicative of a C_4-symmetry preserving structural evolution with reducing temperature. Indeed, inducing a spin-orbit mediated hybridization gap by lifting C_n rotational symmetry would be expected to transform the dispersion of the Dirac cone in the vicinity of the bulk Dirac point from a hyperbolic (i.e., Dirac) dispersion to a more parabolic dispersion [6]. This does not occur in the present case, as evidenced by the near-rigid shift of the full band dispersion in Figs. 3(a) and 3(b), rather than an evolution of the bands themselves. Furthermore, the energy scales of the band shifts are much larger than those found in other semimetallic systems that undergo Lifshitz transitions with temperature, such as WTe$_2$ [47] and ZrTe$_5$ [48]. In Figs. 3(c) and 3(d), we quantify this shift by extracting the energy of the bulk Dirac point as a function of temperature from both the energy-distribution curves in Fig. 3(c), and through an extrapolation of the linear band dispersions extracted from momentum-distribution curves similar to

those shown in Figs. 2(f)–2(j). The result of this analysis is shown in Fig. 3(d), evidencing a shift on the order of ≈ 450 meV when cooling from 300 to 38 K. From Fermi-Dirac statistics and taking into account the calculated density of states, we estimate that the temperature-induced shift of chemical potential over this temperature range is at most ≈ 10 meV, consistent with the energy scale of the band shifts observed in WTe_2 and $ZrTe_5$. The shift of the Dirac point shown in Fig. 3(d) is an order of magnitude larger than this, suggesting a distinct origin for the Lifshitz transition in Au_2Pb compared to those driven by a temperature-induced shift of chemical potential in other semimetals [47–53].

Instead, the Lifshitz transition is driven by a C_4-preserving evolution of the lattice with reducing temperature, resulting in enhanced orbital overlap, and hence a change in the crystal field strengths and hopping parameters that underpin the energetics of a band structure. To further demonstrate this, inset in Fig. 3(d), we show how the experimental lattice parameter [28] behaves in tandem with the energetics of bulk Dirac point with changing temperature, establishing a direct proportionality between the compression of the lattice and the shift of the bulk Dirac point to higher binding energy. In Fig. 4, we perform DFT band structure calculations as a function of lattice compression. The Fermi level is pinned to the Dirac point in the equilibrium structure [Fig. 4(a)]. With continued compression, the Dirac point remains entirely ungapped, but its position clearly shifts to higher binding energy in excellent qualitative agreement with the experiment. We note that, in order to match the experimental shift of the Dirac point, a compression on the order of 2.5% is required, more than the $\approx 1\%$ confirmed experimentally. We attribute this discrepancy to be largely due to an increasing bonding-antibonding splitting due to the proximity of the observed phase transitions and the insufficient consideration of correlation effects (Coulomb interaction) in conventional DFT [54]. Nevertheless, these calculations fully support a compression-induced Lifshitz transition of the bulk Dirac points in Au_2Pb.

In conclusion, the direct experimental observation of bulk Dirac fermions unambiguously establishes cubic Au_2Pb as a stable three-dimensional Dirac semimetal with fourfold degenerate Dirac crossings protected by rotational lattice symmetry. With cooling into the intermediate temperature regime, the linear dispersion forming the BDC undergoes a continuous energetic shift to higher binding energy, driving a Lifshitz transition consistent with a compression of the lattice. Despite the numerous structural phase transitions previously observed to exist in this intermediate temperature regime, this experimental observation evidences both that there is an intact C_4 symmetry component throughout this regime, and that the large compressive perturbation of the lattice is unable to unwind the band crossing altogether, in line with the single-orbital manifold origin of the Dirac cone. The energy scale of the band shifts is an order of magnitude larger than those reported in other semimetals, driven here by an enhanced orbital overlap due to the shrinking of the cubic lattice parameter with reducing temperature. Further structure-preserving modifications, such as partial Pb substitution, may reduce the signal from bulk Fermi crossings away from the Dirac cone while preserving the functionality shown here for Au_2Pb. The present findings underpin new avenues towards *in situ* tuning of Dirac node contributions to transport, both for the fundamental study of Dirac and Weyl fermions, and for applications in next-generation electronic and spintronic devices.

---

*Corresponding author.
jaime.sanchez-barriga@helmholtz-berlin.de

[1] N. P. Armitage, E. J. Mele, and A. Vishwanath, Rev. Mod. Phys. **90**, 015001 (2018).

[2] Z. Wang, Y. Sun, X.-Q. Chen, C. Franchini, G. Xu, H. Weng, X. Dai, and Z. Fang, Phys. Rev. B **85**, 195320 (2012).

[3] Z. Wang, H. Weng, Q. Wu, X. Dai, and Z. Fang, Phys. Rev. B **88**, 125427 (2013).

[4] Z. K. Liu, B. Zhou, Y. Zhang, Z. J. Wang, H. M. Weng, D. Prabhakaran, S.-K. Mo, Z. X. Shen, Z. Fang, X. Dai *et al.*, Science **343**, 864 (2014).

[5] S. Borisenko, Q. Gibson, D. Evtushinsky, V. Zabolotnyy, B. Büchner, and R. J. Cava, Phys. Rev. Lett. **113**, 027603 (2014).

[6] Z. K. Liu, J. Jiang, B. Zhou, Z. J. Wang, Y. Zhang, H. M. Weng, D. Prabhakaran, S.-K. Mo, H. Peng, P. Dudin, T. Kim, M. Hoesch, Z. Fang, X. Dai, Z. X. Shen, D. L. Feng, Z. Hussain, and Y. L. Chen, Nat. Mater. **13**, 677 (2014).

[7] M. Neupane, S.-Y. Xu, R. Sankar, N. Alidoust, G. Bian, C. Liu, I. Belopolski, T.-R. Chang, H.-T. Jeng, H. Lin *et al.*, Nat. Commun. **5**, 3786 (2014).

[8] T. Liang, Q. Gibson, M. N. Ali, M. Liu, R. J. Cava, and N. P. Ong, Nat. Mater. **14**, 280 (2015).

[9] Y. Sun, Y. Zhang, C. Felser, and B. Yan, Phys. Rev. Lett. **117**, 146403 (2016).

[10] S. M. Young, S. Zaheer, J. C. Y. Teo, C. L. Kane, E. J. Mele, and A. M. Rappe, Phys. Rev. Lett. **108**, 140405 (2012).

[11] U. R. Singh, M. Prada, V. Strenzke, B. Bosnjak, T. Schmirander, L. Tiemann, and R. H. Blick, Phys. Rev. B **102**, 245134 (2020).

[12] Y. Yao, F. Ye, X.-L. Qi, S.-C. Zhang, and Z. Fang, Phys. Rev. B **75**, 041401(R) (2007).

[13] B.-J. Yang and N. Nagaosa, Nat. Commun. **5**, 4898 (2014).

[14] J. Xiong, S. K. Kushwaha, T. Liang, J. W. Krizan, M. Hirschberger, W. Wang, R. J. Cava, and N. P. Ong, Science **350**, 413 (2015).

[15] S.-Y. Xu, C. Liu, S. K. Kushwaha, R. Sankar, J. W. Krizan, I. Belopolski, M. Neupane, G. Bian, N. Alidoust, T.-R. Chang *et al.*, Science **347**, 294 (2015).

[16] H. Huang, S. Zhou, and W. Duan, Phys. Rev. B **94**, 121117(R) (2016).

[17] G. Bian, T.-R. Chang, R. Sankar, S.-Y. Xu, H. Zheng, T. Neupert, C.-K. Chiu, S.-M. Huang, G. Chang, I. Belopolski, D. S. Sanchez, M. Neupane, N. Alidoust, C. Liu, B. Wang, C.-C. Lee, H.-T. Jeng, C. Zhang, Z. Yuan, S. Jia, A. Bansil, F. Chou, H. Lin, and M. Z. Hasan, Nat. Commun. **7**, 10556 (2016).

[18] A. Pariari and P. Mandal, Sci. Rep. **7**, 40327 (2017).

[19] P.-J. Guo, H.-C. Yang, K. Liu, and Z.-Y. Lu, Phys. Rev. B **95**, 155112 (2017).

[20] B. Q. Lv, Z. L. Feng, Q. N. Xu, X. Gao, J. Z. Ma, L. Y. Kong, P. Richard, Y. B. Huang, V. N. Strocov, C. Fang, H. M. Weng, Y. G. Shi, T. Qian, and H. Ding, Nature **546**, 627 (2017).

[21] T.-R. Chang, S.-Y. Xu, D. S. Sanchez, W.-F. Tsai, S.-M. Huang, G. Chang, C.-H. Hsu, G. Bian, I. Belopolski, Z.-M. Yu, S. A. Yang, T. Neupert, H.-T. Jeng, H. Lin, and M. Z. Hasan, Phys. Rev. Lett. **119**, 026404 (2017).

[22] H. Huang, K.-H. Jin, and F. Liu, Phys. Rev. B **98**, 121110 (R) (2018).

[23] L. Congcong, W. Xianxin, Q. Shengshan, L. Yinxiang, T. Ronny, Z. Fu-Chun, and H. Jiangping, Proc. Natl. Acad. Sci. U.S.A. **115**, 8311 (2018).

[24] P. Zhang, Z. Wang, X. Wu, K. Yaji, Y. Ishida, Y. Kohama, G. Dai, Y. Sun, C. Bareille, K. Kuroda, T. Kondo, K. Okazaki, K. Kindo, X. Wang, C. Jin, J. Hu, R. Thomale, K. Sumida, S. Wu, K. Miyamoto, T. Okuda, H. Ding, G. D. Gu, T. Tamegai, T. Kawakami, M. Sato, and S. Shin, Nat. Phys. **15**, 41 (2019).

[25] T. Y. Yang, Q. Wan, D. Y. Yan, Z. Zhu, Z. W. Wang, C. Peng, Y. B. Huang, R. Yu, J. Hu, Z. Q. Mao, S. Li, S. A. Yang, H. Zheng, J. F. Jia, Y. G. Shi, and N. Xu, Nat. Mater. **19**, 27 (2020).

[26] O. J. Clark, F. Mazzola, I. Marković, J. M. Riley, J. Feng, B.-J. Yang, K. Sumida, T. Okuda, J. Fujii, I. Vobornik, K. T. K., K. Okawa, T. Sasagawa, M. S. Bahramy, and K. P. D. C., Electron. Struct. **1**, 014002 (2019).

[27] B. J. Wieder, B. Bradlyn, J. Cano, Z. Wang, M. G. Vergniory, L. Elcoro, A. A. Soluyanov, C. Felser, T. Neupert, N. Regnault, and B. A. Bernevig, Nat. Rev. Mater. **7**, 196 (2022).

[28] L. M. Schoop, L. S. Xie, R. Chen, Q. D. Gibson, S. H. Lapidus, I. Kimchi, M. Hirschberger, N. Haldolaarachchige, M. N. Ali, C. A. Belvin *et al.*, Phys. Rev. B **91**, 214517 (2015).

[29] K. W. Chen, D. Graf, T. Besara, A. Gallagher, N. Kikugawa, L. Balicas, T. Siegrist, A. Shekhter, and R. E. Baumbach, Phys. Rev. B **93**, 045118 (2016).

[30] M. Sato and Y. Ando, Rep. Prog. Phys. **80**, 076501 (2017).

[31] O. J. Clark, M. J. Neat, K. Okawa, L. Bawden, I. Marković, F. Mazzola, J. Feng, V. Sunko, J. M. Riley, W. Meevasana,

J. Fujii, I. Vobornik, T. K. Kim, M. Hoesch, T. Sasagawa, P. Wahl, M. S. Bahramy, and P. D. C. King, Phys. Rev. Lett. **120**, 156401 (2018).

[32] L. Kong, L. Cao, S. Zhu, M. Papaj, G. Dai, G. Li, P. Fan, W. Liu, F. Yang, X. Wang, S. Du, C. Jin, L. Fu, H.-J. Gao, and H. Ding, Nat. Commun. **12**, 4146 (2021).

[33] Y. Wu, G. Drachuck, L.-L. Wang, D. D. Johnson, P. Swatek, B. Schrunk, D. Mou, L. Huang, S. L. Bud'ko, P. C. Canfield, and A. Kaminski, Phys. Rev. B **98**, 161107(R) (2018).

[34] A. Varykhalov, O. Rader, and W. Gudat, Phys. Rev. B **72**, 115440 (2005).

[35] P. Blaha, K. Schwarz, G. K. H. Madsen, D. Kvasnicka, and J. Luitz, WIEN2k, *An Augmented Plane Wave + Local Orbitals Program for Calculating Crystal Properties* (Karlheinz Schwarz, Techn. Universität Wien, Austria, 2001).

[36] Y. Xing, H. Wang, C.-K. Li, X. Zhang, J. Liu, Y. Zhang, J. Luo, Z. Wang, Y. Wang, L. Ling, M. Tian, S. Jia, J. Feng, X.-J. Liu, J. Wei, and J. Wang, npj Quantum Mater. **1**, 16005 (2016).

[37] S. Hüfner, *Very High Resolution Photoelectron Spectroscopy* (Springer-Verlag Berlin Heidelberg, 2007).

[38] I. M. Lifshitz, Sov. Phys. JETP **11**, 1130 (1960).

[39] Y. Li, Y. Xia, S. A. Ekahana, N. Kumar, J. Jiang, L. Yang, C. Chen, C. Liu, B. Yan, C. Felser, G. Li, Z. Liu, and Y. Chen, Phys. Rev. Mater. **1**, 074202 (2017).

[40] M. S. Bahramy, O. J. Clark, B.-J. Yang, J. Feng, L. Bawden, J. M. Riley, M. I., F. Mazzola, V. Sunko, D. Biswas, S. P. Cooil, M. Jorge, J. W. Wells, M. Leandersson, T. Balasubramanian, J. Fujii, I. Vobornik, J. Rault, T. K. Kim, M. Hoesch, K. Okawa, M. Asakawa, T. Sasagawa, T. Eknapakul, W. Meevasana, and P. D. C. King, Nat. Mater. **17**, 21 (2018).

[41] C. Nicholson, M. Rumo, A. Pulkkinen, G. Kremer, B. Salzmann, M.-L. Mottas, B. Hildebrand, T. Jaouen, T. K. Kim, S. Mukherjee, K. Ma, M. Muntwiler, F. O. von Rohr, C. Cacho, and C. Monney, Commun. Mater. **2**, 25 (2021).

[42] B. Ghosh, D. Mondal, C.-N. Kuo, C. S. Lue, J. Nayak, J. Fujii, I. Vobornik, A. Politano, and A. Agarwal, Phys. Rev. B **100**, 195134 (2019).

[43] S. Mukherjee, S. W. Jung, S. F. Weber, C. Xu, D. Qian, X. Xu, P. K. Biswas, T. K. Kim, C. L. C., M. D. Watson, J. B. Neaton, and C. Cacho, Sci. Rep. **10**, 12957 (2020).

[44] L. Kong and H. Ding, Acta Phys. Sin. **69**, 110301 (2020).

[45] R. C. Xiao, P. L. Gong, Q. S. Wu, W. J. Lu, M. J. Wei, J. Y. Li, H. Y. Lv, X. Luo, P. Tong, X. B. Zhu, and Y. P. Sun, Phys. Rev. B **96**, 075101 (2017).

[46] F. Fei, X. Bo, P. Wang, J. Ying, J. Li, K. Chen, Q. Dai, B. Chen, Z. Sun, M. Zhang, F. Qu, Y. Zhang, Q. Wang, X. Wang, L. Cao, H. Bu, F. Song, X. Wan, and B. Wang, Adv. Mater. **30**, 1801556 (2018).

[47] Y. Wu, N. H. Jo, M. Ochi, L. Huang, D. Mou, S. L. Bud'ko, P. C. Canfield, N. Trivedi, R. Arita, and A. Kaminski, Phys. Rev. Lett. **115**, 166602 (2015).

[48] Y. Zhang, C. Wang, L. Yu, G. Liu, A. Liang, J. Huang, S. Nie, X. Sun, Y. Zhang, B. Shen *et al.*, Nat. Commun. **8**, 15512 (2017).

[49] Y. Zhang *et al.*, Sci. Bull. **62**, 950 (2017).

[50] F. C. Chen, Y. Fei, S. J. Li, Q. Wang, X. Luo, J. Yan, W. J. Lu, P. Tong, W. H. Song, X. B. Zhu, L. Zhang, H. B. Zhou,

F. W. Zheng, P. Zhang, A. L. Lichtenstein, M. I. Katsnelson, Y. Yin, N. Hao, and Y. P. Sun, Phys. Rev. Lett. **124**, 236601 (2020).

[51] Y. Jian, Q. Wu, M. Yang, Q. Feng, J. Duan, D. Chen, Q. Wang, W. Xiao, Y. Shi, O. V. Yazyev, and Y. Yao, 2D Mater. **8**, 015020 (2020).

[52] S. Y. Back, Y.-K. Kim, H. Cho, M.-K. Han, S.-J. Kim, and J. S. Rhyee, ACS Appl. Energy Mater. **3**, 3628 (2020).

[53] X. Wang, D. Pan, Q. Zeng, X. Chen, H. Wang, D. Zhao, Z. Xu, Q. Yang, J. Deng, T. Zhai, G. Wu, E. Liu, and J. Zhao, Nanoscale **13**, 2601 (2021).

[54] J. P. Perdew and A. Zunger, Phys. Rev. B **23**, 5048 (1981).